

PHYSICAL EFFECTS OF GAS ENVELOPES WITH DIFFERENT EXTENSION ON THE COLLAPSE OF A GAS CORE.

Guillermo Arreaga-García¹ and Julio Saucedo Morales,¹

Draft version: October 2, 2018

RESUMEN

En este trabajo estudiamos el colapso gravitacional de una nube de gas de hidrógeno molecular compuesta de un núcleo más un envoltente de gas rodeando al núcleo. Simulamos numéricamente el colapso de cuatro modelos de nube para entrever la evolución temporal de algunas variables dinámicas, entre otras, el momento angular y la razón aem ; las razones entre las energías térmica y rotacional con respecto a la energía potencial gravitacional, denotadas como α y β , respectivamente. Re-tomamos los modelos introducidos por Arreaga et al. (2010), para hacer una caracterización cuantitativa de los diferentes resultados del colapso de la nube por medio de las variables dinámicas ya mencionadas. Mostramos que podemos comparar cuantitativamente los efectos de la extensión del envoltente de gas sobre el colapso del núcleo.

ABSTRACT

In this paper we study the gravitational collapse of a molecular hydrogen gas cloud composed of a core plus a gas envelope surrounding the core. We numerically simulate the collapse of four cloud models to take a glimpse to the time evolution of several dynamic variables, such as the angular momentum and the aem ratio, as well as the ratios between the thermal and rotational energies with respect to the potential gravitational energy, denoted as α and β , respectively, among others. We re-take those models introduced by Arreaga et al. (2010) in the present paper in order to produce different outcomes of the collapsing cloud characterized in terms of the aforementioned dynamical variables. Such characterization was missing in the paper by Arreaga et al. (2010), and here we show that the gas envelope extension effects on the collapsing core can be quantitatively compared.

Key Words: dynamical variables — integral properties — collapse

1. INTRODUCTION

It is suggested by observational evidence that most young stars in the Galaxy (around 50%) are coupled in binary systems. Astronomical observations and theoretical studies point out to the clouds early fragmentation as the leading mechanism to explain the binary stellar systems origin and properties (see the review by Bodenheimer et al. (2000), where several theoretical mechanisms for binary formation are discussed). Thus, fragmentation is a very

¹Centro de Investigación en Física de la Universidad de Sonora, Mexico.

important physical phenomenon whose occurrence in clouds is paramount. Indeed, cloud fragmentation is one of the key physical events that any plausible theory of star formation must include, in order to explain the observed property that most new born stars are clustered in binary or multiple groups.

Recently, Arreaga et al. (2010) have studied the protostellar clouds gravitational collapse, including rotation, thermal pressure and a centrally condensed radial density profile. They considered a cloud model composed of a core plus a gas envelope surrounding it; they reported the outcome of a cloud model depending on both the extension and mass of the gas envelope. The novel idea that these authors worked out was the change of the radial extension of the outer envelope.

In this paper we focus on trying to quantitatively characterize the most important dynamical events of the full three dimensional set of numerical hydrodynamical simulations introduced by Arreaga et al. (2010). We consider again those cloud models to achieve such a goal, focusing now on some dynamical variables, mainly on the acceleration, density, specific angular momentum J/M and the *aem* ratio² $aem \equiv \frac{cJ}{GM^2}$, as well as in the ratios between the thermal and rotational energies with respect to the gravitational potential energy, denoted by α and β , respectively. We prove here that these dynamic variables characterize rather well the collapse process by capturing the most representative physical events, including fragmentation, which leaves an imprint on these dynamical variables. It must be noted that the *aem* ratio is a dimensionless measure of the specific angular momentum, which fortunately has been estimated for protostellar clouds. For instance, Felice & Sigalotti (1992) reported that protostellar cores around one solar mass have an *aem* ratio of about 10^5 . We use here this *aem* ratio for measuring the redistribution of mass and angular momentum during the cloud collapse, particularly in its central region. The general result obtained is the systematic decrease of the *aem* ratio for the particles involved in the central cloud collapse.

It must be emphasized that no plots with integral or mechanical properties of the cloud models were reported in the paper by Arreaga et al. (2010). This absence is now the main concern for the present work, which must be considered as an extension of the work by Arreaga et al. (2010), as we now study how the different collapsing outcomes are manifested on the dynamic variables. Consequently, we include several plots to envisage the cloud mechanical state as the gravitational collapse takes place. Hence, we expect that the physical characterization of the models, and above all, the integral properties calculation, will be useful for a better understanding of the physics of the gravitational collapse.

Let us recall that there are several papers demonstrating that the fate of a collapsing cloud is ultimately determined by the initial values of its α and β energy ratios, see for instance Tsuribe (2002) and references therein. Thus, for allowing a comparison to be made between our models and those of other authors, we have set fixed values chosen from the collapse literature to these

²Where c is the speed of light and G is the Newton gravitational constant.

ratios for all our cloud models. Furthermore, since all the clouds considered in the paper hereby have the same radial density profile, we find ourselves in a good position to study the different gas envelopes effects on the collapse of a unique central gas core, as all the models share the same innermost central density region.

We mention that one of the most relevant effects of the envelopes on the collapsing core is the different extension of the spiral arms that develop around the densest clump, that forms at the cloud central region. Thus, the results of our models provide a representative sample of scenarios composed by a central clump plus spiral arms of different lengths.

Recently, Tsukamoto & Machida (2011) carried out a large set of simulations whose outcomes span a wide sample of stellar systems formed by a central protostar plus a surrounding gas disk. Indeed, our sample is a subset of reported by Tsukamoto & Machida (2011), but in our case, we only need to deal with a single value for each of the α and β energy ratios, whereas these authors used a wide range of pairs of values to characterize many independent clouds. Therefore, we can consider that we have the same cloud collapsing several times to produce different outcomes, which can be attributed mainly to the different extension of the gas envelope, this means we only need to smoothly change the cloud conditions in order to see new physical scenarios resulting from the collapse.

Moreover, the nature of the disk-star system can have a very deep influence on the star formation process by means of the disk interaction with the central star through gravitational torques, as it was demonstrated by Lin et al. (2011). One of the most interesting results that these authors found was that the central protostar spin rate is remarkably reduced by the action of gravitational forces upon it. They argued that the evolution of the central protostar angular momentum is strongly influenced by the external fluid surrounding it.

We track the paths of the particles entering into the central clump during the simulation in the paper hereby, looking forward to see how those particles lose angular momentum, as a consequence of both the shear viscosity and the gravitational potential lines rearrangement caused by the bar-like deformations in the geometry of the densest central mass distribution. We particularly show how the dynamical orbital angular momentum and the *aem* ratio are assembled from the properties of the individual particles. These orbital properties are also ultimately regulated by the gas envelope extension.

The outline of the paper is as follows. In Section 2 we present in detail the cloud models of Arreaga et al. (2010), which are studied in this paper too, enable a better reading. We introduce the behavior of the most familiar dynamical variables relevant to the collapsing cloud in Section 3, namely: mass, density, acceleration, angular momentum and the energy ratios. Later, we discuss how the different outcomes of the cloud models are recorded on some of the aforementioned dynamical variables. We try to explain the most relevant physical events during the collapse, in Section 4, in terms of the dy-

TABLE 1
THE COLLAPSE MODELS.

Model	$\frac{R_0}{R_c}$	M_0 gr	ρ_0 gr/cm^3	Ω_0 $\times 10^{-13}$ rad/sec	c_0 cm/sec
A0	0.5	6.28×10^{32}	2.23×10^{-18}	5.80	10620.35
A1	1.5	5.14×10^{33}	6.95×10^{-19}	3.90	18751.51
A2	2.5	8.34×10^{33}	2.43×10^{-19}	2.95	19942.80
A3	3.7	1.04×10^{34}	9.22×10^{-20}	2.22	20344.14

namical variables behavior describing the cloud evolution. Finally, we remark the importance that the results of a simulation can eventually be explained in terms of its dynamical variables in Sect.5.

2. INITIAL CONDITIONS OF THE SUITE OF CLOUD MODELS

As we aim to study the gas envelope effects on the core collapse quantitatively, we consider four cloud models labeled as A0, A1, A2 and A3, each with different extension of the envelope relative to the core radius, that is, $R_0/R_c = 0.5, 1.5, 2.5$ and 3.7 , respectively, where R_0 is the cloud radius and R_c the core radius. We illustrate that the cloud models under consideration are centrally condensed in the left panels of Figs.1 and 2; we summarize the values of the most important physical parameters used for setting up these models in Table 1.

2.1. The initial radial density profile.

Protostellar collapse models with central condensations were first studied by Boss (1987), Boss (1991) and subsequently by Sigalotti & Klapp (1994) and Sigalotti & Klapp (1996), among others. In fact, the model of a centrally condensed cloud studied by Arreaga et al. (2010) has been called a Plummer cloud, because the radial density profile used for the cloud was inspired in the following Plummer-like function

$$\rho(r) = \rho_c \left(\frac{R_c}{\sqrt{r^2 + R_c^2}} \right)^\eta, \quad (1)$$

where we have fixed the free parameters to the following values:

$$\begin{aligned} \rho_c &= 3.0 \times 10^{-18} \text{ gr cm}^{-3} = 8.96 \times 10^5 \text{ molecules cm}^{-3}, \\ R_c &= 8.06 \times 10^{16} \text{ cm} = 0.026 \text{ pc}, \\ \eta &= 4. \end{aligned} \quad (2)$$

as suggested by Whithworth & Ward-Thompson (2001).

We have added the labels $A0$, $A1$, $A2$ and $A3$ in the plots, to indicate the cutting radii of the Plummer cloud, whose different extensions define each of the simulation models, as illustrated in the right panel of Fig.2. We mention that the density curves in the right panel of Fig.1 show slight and unimportant differences in the cloud central region (near the $A0$ label). As all the clouds share the same radial density profile in its innermost parts, then we consider that all the cloud models share the same core, despite of the fact that the models differ in other physical parameters, such as the angular velocity.

We also mention that the radial Plummer function shown in Eq.1 does not "exactly" satisfy the isothermal Lane-Emden equation, which determines the solution for an isothermal cloud in an equilibrium configuration. However, what is most important for us is that the qualitative behavior of the Plummer-like profile behaves very similar to an approximate analytic solution of the Lane-Emden equation for the isothermal sphere, as it was found by Natarayan and Lynden-Bell (1997); their approximate solution is accurate within 0.04% with the Plummer density profile.

By comparing the Fig. 1 of Natarayan and Lynden-Bell (1997) with the right panel of our Fig. 1, we conclude that these functions behave mathematically almost identically. Moreover, as it was demonstrated by Whithworth & Ward-Thompson (2001), what becomes more useful after considering the Plummer profile as a model of protostellar collapse, is that the physical quantities have simple analytic forms, thus avoiding numerical methods as the only tool of analysis. Consequently, we have found it to be worthwhile to consider simulations with the Plummer radial density profile.

2.2. The initial assembly of particles.

We have accomplished to have a set of $N = 10$ million *SPH* particles representing the initial cloud configuration with the aforementioned radial density profile. It should be noticed that the *SPH* particles do not always have the same mass m_i in a simulation, for two reasons. The first is that each particle mass is determined by its coordinates location (x_i, y_i, z_i) , according to the density profile, that is, $m_i = \rho(x_i, y_i, z_i) * \Delta x \Delta y \Delta z$ with $i = 1, \dots, N$, where Δx indicates the size of each dimension of the rectangular grid in which the particles are initially located. The cloud space volume was covered with a total of 286^3 grid elements. The second reason was that a density perturbation was applied initially by hand to the mass of each *SPH* simulation particle m_i in all of the cloud models according to:

$$m_i = m_0 (1 + a \cos(m \phi_i)) , \quad (3)$$

where m_0 is the mass of the *SPH* simulation particle, and we set the perturbation amplitude to $a = 0.1$, while the mode is fixed to $m = 2$. It was done with the purpose of favoring a binary protostar development in the cloud innermost region at the end of the simulation. These values of m

and a have been chosen as it is customary in this field of work; see for instance, Burkert & Bodenheimer (1993), Burkert & Bodenheimer (1996) and Sigalotti & Klapp (2001).

We show the total mass contained in the Plummer cloud in the right panel of Fig. 2, which is always an increasing function of the cloud radius r . As an accuracy confirmation of our initial particles configuration, the mass calculated from the integration of the Plummer function and from the initial configuration of our *SPH* particles agrees very well, as expected.

2.3. Initial energies.

The initial cloud for all the models considered in this paper is in counter-clockwise rigid body rotation around the z axis; therefore, the initial velocity for the i -th *SPH* particle is given by $\vec{v}_i = \vec{\Omega}_0 \times \vec{r}_i = (-\Omega_0 y_i, \Omega_0 x_i, 0)$, where Ω_0 is the angular velocity magnitude, which has a different value depending on the cloud model, see Table 1.

It is important to emphasize that all of our cloud models initially have the same thermal and rotational energy ratio with regards to the gravitational energy, which are denoted by α_0 and β_0 , respectively³. As a matter of fact, in Table 1 we have also reported the initial sound speed c_0 and the initial angular velocity Ω_0 given to each cloud model in order to have the following numerical ratios:

$$\begin{aligned} \alpha_0 &\equiv \frac{E_{therm}}{|E_{grav}|} = 0.26 , \\ \beta_0 &\equiv \frac{E_{rot}}{|E_{grav}|} = 0.16 . \end{aligned} \tag{4}$$

These α_0 and β_0 values were chosen to allow a direct comparison with other authors, see for example Bodenheimer et al. (2000). Regarding our models, the $\beta_0 = 0.16$ value gives a cloud angular velocity $\Omega_0 \sim (2.22 - 5.80) \times 10^{-13} \text{ s}^{-1}$; for the case of the uniform density standard isothermal test, $\alpha_0 = 0.25$ and $\beta_0 = 0.20$ that gives $\Omega_0 = 1.56 \times 10^{-12} \text{ s}^{-1}$ (see Boss & Bodenheimer (1979) and Sigalotti & Klapp (1997)), which is an order of magnitude higher than our β_0 range values.

We calculate the energy ratios for the core alone in order to illustrate the energy sharing mechanism between the core and the envelope, neglecting those particles whose distance to the cloud center is greater than R_c ; we ignore all the *SPH* particles whose radius coordinate r_i is $r_i > R_c$. The results are presented in Table 2, where the α_c and β_c values are calculated up to the core radius R_c . As expected, according to Table 2 the core dynamical properties for the initial configuration in model *A0* are identical to the whole cloud dynamical properties, as set by Eq.4. Another observation from Table 2 is that the larger the gas envelope, the greater the core thermal energy and, at the same time, the core rotational energy is smaller. This statement will

³See Sect.3.5.2 for a detailed definition of α and β in the frame of the *SPH* technique.

TABLE 2
ENERGY RATIOS CALCULATED UP TO THE CORE RADIUS.

Model	α_c	β_c	$\alpha_c + \beta_c$
A0	0.2643	0.1618	0.4261
A1	0.3002	0.1114	0.4116
A2	0.3350	0.0657	0.4007
A3	0.3547	0.0374	0.3921

have important consequences to explain the different outcomes derived from the simulations, as it will be seen in Section 3.5.4.

It is also noteworthy to appreciate by looking at the third column of Table 2, that the sum of the energy ratios is always below 0.5 for all models. This feature is important as it sets the cloud general tendency to collapse, as dictated by the virial theorem, which would apply if the hydrogen cloud were in thermodynamical equilibrium. If this was the case, the energy ratios would satisfy the virial equation.

$$\alpha + \beta = \frac{1}{2}, \quad (5)$$

a relation which will be used in some of the plots of the following sections.

2.4. *The equation of state.*

Once gravity has produced a substantial contraction of the cloud, the gas begins to heat. We use a barotropic equation of state in order to take this fact into account, as it was originally proposed by Boss et al. (2000), to model the gas thermodynamics:

$$p = c_0^2 \rho \left[1 + \left(\frac{\rho}{\rho_{crit}} \right)^{\gamma-1} \right], \quad (6)$$

where ρ_{crit} defines the critical density above which the collapse changes from isothermal to adiabatic, and for a molecular hydrogen gas the ratio of specific heats is $\gamma \equiv 5/3$. Furthermore, in this paper we consider only the value

$$\rho_{crit} = 5.0 \times 10^{-14} \text{ gr/cm}^3, \quad (7)$$

chosen to allow a direct comparison with Boss et al. (2000), who calculated a uniform and gaussian cloud with a barotropic equation of state considering the Eddington approximation.

2.5. *Initial angular momentum.*

The importance of studying the origin of the angular momentum has been reviewed by Bodenheimer (1995) and Zinnecker (2004). In fact, the observed

values of J/M and aem for pre-main sequence stars are lower than those observed for typical rotating protostellar cores, implying that mass and angular momentum should be redistributed somehow to ensure a decrease of the J/M and aem by factors of 10^3 to 10^4 during star formation, see also Sigalotti & Klapp (1994).

It must also be mentioned that observations by Goodman et al. (1993) have shown that dense cores have velocity gradients of about 0.3 to $4.0 \text{ km s}^{-1} \text{ pc}^{-1}$, which correspond to angular velocities in the range of $\Omega_0 \sim 9.6 \times 10^{-15} \text{ s}^{-1}$ to $\sim 1.2 \times 10^{-13} \text{ s}^{-1}$, values which are slightly below ours.

The observational relation between angular momentum and the cloud radius for molecular cores has been reported by Goodman et al. (1993) (see their Fig. 13). Indeed, this plot has been reproduced and improved by Bodenheimer (1995) in his Fig. 1. Let us consider for instance our model A3, with $R_0 = 0.097 \text{ pc}$; an associated specific angular momentum $j = 6.3 \times 10^{21} \text{ cm}^2 \text{ s}^{-1}$, which corresponds to an angular velocity $\Omega = 1.75 \times 10^{-13} \text{ s}^{-1}$; a value which is very close to ours for model A3. Hence, as suggested by observations, our angular velocity range is also similar to their numerical simulations.

The specific total angular momentum for all the initial configuration of particles defining our models, is shown in Fig. 3. We have introduced asterisks in Fig.3 to mark the observed quantities to make clear that the dynamical properties of our clouds are typical when compared with the observations reported by Goodman et al. (1993) and Bodenheimer (1995).

Curiously, for the initial configuration of model A0 there is no gas envelope, as the cloud extends only to $R_c/2$. Model A0 has the highest initial density and the highest rotational speed because it has the smallest cloud size, as it can be seen in Table 1. Besides, its specific angular momentum is lower than those already observed for protostellar clouds, see Fig. 3. The results of this simulation are rather interesting, as its dynamical evolution is similar to that calculated for the uniform density cloud models, that is, a cloud with $\rho(r) = \rho_0$ for all r , see for instance Arreaga et al. (2007, 2008).

3. PHYSICAL CHARACTERIZATION

We will discuss the behavior of some of the most important dynamical variables related with the cloud collapse in the forthcoming subsections. When necessary, we will restrict ourselves to consider only the initial and final snapshots available in each simulation, as an approximation to a complete time evolution of a dynamical variable. It should be noted that the simulations were evolved by Arreaga et al. (2010) a little longer than we do for this paper.

As we will notice in Section 3.1, in order to study the results of the simulations, it is enough to make iso-density plots for a slice of particles around the cloud's equatorial plane. We present in Figs. 5, 6, 7 and 8 the main results of the models to show the marked differences for each model. A more complete sets of results has already been presented by Arreaga et al. (2010).

3.1. The cloud flattening

The Plummer density profile assembles a very peculiar mass distribution; as it is pulled down by the force of gravity towards the cloud center against the combined effect of rotation and pressure, see Fig. 4.

The centripetal acceleration is given by $a_c = R_{\perp}\Omega$ for the spherical cloud in rigid rotation with respect to the Z -axis, where R_{\perp} is the shortest distance from the particle to the rotation axis. As $R_{\perp} = R_0 * \sin(\theta)$, where θ is the polar spherical angle, then we have that a_c has its maximum value at the equator (where $\theta = \pi/2$) and its minimum value at the poles (where $\theta = 0$).

Every particle feels a centripetal acceleration, at least in the local reference frame located on the particle, as a radial force, always opposing the radially attractive gravitational force. Thus, due to the fact that this centrifugal force along the equator of the cloud is greater than at the poles, the cloud contraction is faster at the poles than at the equator; then the cloud evolves through a sequence of flatter configurations parallel to the cloud equator and perpendicular to the rotation axis. Numerical simulations performed so far have proved that a uniformly rotating molecular cloud, similar to the one considered here, contracts itself in its innermost region during the isothermal regime to an almost flat configuration, see for instance Burkert & Bodenheimer (1993, 1996) and Sigalotti & Klapp (2001).

3.2. Mass and density.

According to the left panel of Fig. 4, initially more mass is accumulated within the core boundary than in the gas envelope. As expected, after most of the collapse has taken place, most of the mass had already accumulated in the cloud center, as it can be seen in the right panel of Fig. 4, where we show the mass radial profile for the last snapshot.

There is a characteristic time scale for the cloud collapse, which is given by

$$t_{ff} \approx \sqrt{\frac{3\pi}{32G\rho}}. \quad (8)$$

The free fall scale time t_{ff} is defined by a characteristic cloud density ρ . If we use the cloud average density ρ_0 , the t_{ff} will correspond to the time for a test particle falling freely from the cloud surface to the cloud center. As our models have an increasing radius, then the time we expect for the cloud to collapse ranges from 8 744 *years* for model A0; 45 436 *years* for model A1; 97 764 *years* for model A2 to 177 603 *years* for model A3. As we prefer to have only one scale time to normalize the collapse history of all clouds, then we use the central core density, ρ_c , which allows us to define the time $t_{ffc} = 38\,460$ *years*.

There is clearly a first evolution stage, as it can be seen in Fig. 9, in which the collapse proceeds very slowly until the time has almost reached $t \approx t_{ffc}$. Shortly after, a stage of a more rapid density increase begins in which

the peak density increases in a significant manner until $\rho_{max} \approx \rho_c \times 10^7 \approx 3 \times 10^{-11} \text{ gr/cm}^3$.

The model *A3* collapse takes a longer time than the others because it has more pressure support, more mass and more envelope extension than the other models. Additionally, we note that a smaller number of particles in model *A3* achieves higher densities than in model *A0*, as illustrated in the right panel of Figure 9, where a particle distribution characterized by the peak density is shown for the last snapshot available in each simulation. To interpret this plot, consider a vertical line, as the one labeling the fraction $f = 0.8$; then, this means that 80% of the particles in model *A0* have a density greater than $\log_{10}(\rho_{max}/\rho_0) \approx 2$, which translates into $\rho_{max} = 3.0 \times 10^{-16} \text{ gr/cm}^3$; whereas in model *A3* for the same fraction of particles, 80% have a density higher than $\rho_{max} = 4.75 \times 10^{-20} \text{ gr/cm}^3$, which is a very low value indeed. We observe therefore that the model *A0* collapses faster than the model *A3*.

3.3. Acceleration.

Let us consider now the acceleration generated by the particular mass distributions assembled in the Plummer clouds. We show the total acceleration radial component evolution as a function of radius in Fig. 10. These accelerations have been calculated by dividing the cloud into a fixed number (30) of spherical shells and averaging the radial accelerations of all the particles contained in the same shell. As it can be seen in the left panel of Fig. 10, the curve has a local minimum, indicating that there is a shell of material which feels the highest gravitational attraction in the cloud.

If r_{min} is the radius of the shell with the highest gravitational pull, then for those shells farther away, that is with $r > r_{min}$, their total acceleration begins to increase making the gravitational force acting on these layers outside the core not very relevant. It was analitically demonstrated by Burkert & Hartmann (2004) that the radial acceleration for $2d$ disks diverges at $r = R_0$, but that for a finite thickness disk, the divergence would not occur.

As expected, the behavior of accelerations show significant differences in the final stage of the collapse process, as it can be appreciated in the right panel of Fig. 10. The hydrodynamic pressure is clearly dominant in the cloud center, where it even shows a clear tendency towards gas expansion. As a consequence of the cloud rigid body rotation, a term of centripetal acceleration $-\Omega^2 r$ appears, directed toward the cloud center, which makes it very difficult to increase the magnitude of the total acceleration.

3.4. Angular momentum and aem ratio.

As there is no external force acting upon the cloud, the total angular momentum must be conserved. We verify this conservation property by summing up all the *SPH* particles of a run: $\vec{J} = \sum_{i=1}^N m_i \vec{r}_i \times \vec{v}_i$, and using all the snapshots obtained in each simulations, as it can be seen in both panels of Fig. 11. We see in this plot that the cloud for model *A0* has the smallest

specific angular momentum, while its *aem* ratio is the highest. These values can be easily explained for model A0, because it has less mass and its size is smaller than in the other models. Nevertheless, the *aem* ratio value is almost the same for the rest of the models.

3.4.1. Radial profile.

The angular momentum for a rigid body is given by the $J = I \Omega$ relation, where I is the moment of inertia and Ω is the angular velocity. The cloud in our models is a rigid sphere-like in the initial snapshot; we will now try to generalize this simple mathematical relation to our cloud models for later times. We would have in such case

$$\log_{10}(J/M) = \zeta \log_{10}(r/R_0) + \log_{10}(\Omega) \quad (9)$$

with ζ being a constant. We have also calculated both the angular momentum and the *aem* ratio radial profile, aiming to figure out to what extent this relation remains valid in the cloud evolution. As was done for the acceleration calculation, this task was carried out by dividing the cloud in thin shells, to add the contribution of each particle within the shell afterwards, so that at the end of the task we end up with the momentum and mass for every shell. We can see, by applying this procedure to the first snapshot of each simulation, that the relation 9 is initially well justified, as it is shown in the left panel of Fig. 12.

Now, in the right panel of Fig. 12 we present the results of the same calculations on shells, but now for the last snapshot available in each simulation. As expected, at the final time of evolution we observe that some kind of differential rotation regime is present, above all, for the cloud outermost regions. At that point, relation 9 is no longer valid, as the cloud geometry and the mass distributions have already changed. Indeed, the cloud moment of inertia has changed somewhat due to the process of material accumulation at the cloud center. The effects of this accretion process look more dramatic for the case of the *aem* ratio radial profile, as it can be seen in Fig. 13. The reason for this behavior is again the mass accumulated in the cloud central region, as the *aem* ratio magnitude within a gas radial shell goes as the squared of the mass; then its magnitude is significantly reduced.

3.4.2. Correlation with the particle peak density.

We change the independent variable in the preceding Figures from cloud radius to density. Let us start by looking at Fig. 14, where we show the specific angular momentum and *aem* ratio distribution against the particle density, in the last snapshot available for each of the different runs. It is clearly seen that as the *SPH* particle eventually acquires a greater density, its momentum and *aem* ratio decrease.

Regardless of the peak density value, the particles are giving up part of their angular momentum as a consequence of both the shear viscosity presence

and the decreasing value of their radial distance \vec{r} to the coordinates origin and, because in some cases, this origin coincides with the center of the cloud densest central region.

Additionally, it is interesting to note that there is a more pronounced drop of the aem ratio in the model $A3$ than for the model $A0$, as it can be seen in the right panel of Fig. 14. Even though the collapse is faster for the model $A0$ than for the model $A3$. Shear effects are probably less important for model $A0$ than for model $A3$, as its mass and velocities observed in the cloud central region are smaller for model $A0$ than for model $A3$, as we will see below.

However, we observe in Fig. 14 that there is a final stage in which the loss of the specific angular momentum and aem ratio is less severe for all the models; furthermore, for the model $A3$ one can see even a trend toward a recovery in the value for the last part of the curves of angular momentum and aem ratio. This behavior can be explained because the envelope of the model $A3$ increases, and its particles are more distant (a larger r) from the center, so their angular momentum must still be higher. There is also another reason, which is due to the appearance of the fragments orbital motion, as will be discussed in Section 3.5.1.

We show the velocity field distribution of all those particles located within the cloud central region in Fig. 15, in order to shed more light into the marked differences obtained at the cloud center, according to the cloud model and at the time reached by the last available snapshot.

3.4.3. Rate of change of the angular momentum with the cloud radius.

Let us end this section by considering the change in the angular momentum radial profile for a particle located initially at $\vec{r} + \Delta\vec{r}$ and moving towards an innermost radial shell \vec{r} . The new angular momentum is

$$\vec{L}(\vec{r} + \Delta\vec{r}) = m(\vec{r} + \Delta\vec{r}) \times (\vec{v} + \Delta\vec{v}) \quad (10)$$

where m is the mass of the particle. Then, replacing the kinematic relations $\Delta\vec{r} = \vec{v}\Delta t$ and $\Delta\vec{v} = \vec{a}\Delta t$ into Eq. 10, we obtain the following differential equations which are valid only to first order,

$$\frac{d\vec{L}(\vec{r})}{dr} = \frac{m}{\dot{r}} \vec{r} \times \vec{a} \quad (11)$$

where \dot{r} is defined as $\frac{dr}{dt}$; this function obviously depends on the very particular way in which the gas particles accretion is taking place. Furthermore, the Eq.11 clearly indicates that there would be no change in the angular momentum with respect to r for models with a purely radial acceleration (as a cloud having all its particles moving in a homogeneous circular motion). There would indeed be a change in the angular momentum only for those particles having a non-zero tangential (centrifugal) acceleration. This would be the case if either shear viscosity is present or if a redistribution of forces occurs in

the cloud central region as a consequence of a change in the clump geometry, as we discuss in Section 4.

It is beyond the limited scope of this paper to consider the equation describing the change of the angular momentum for those particles falling into the cloud center, which tentatively is still an unknown and perhaps very complicated issue. However, we can take advantage of our simulations for measuring the way in which those particles being accreted are losing their angular momentum. We have selected a set of particles for this purpose, which have already reached the cloud innermost region at the last available snapshot for each model. Subsequently, we followed this set of particles -in as many previous snapshots as possible- along their path into the densest central gas clump. As an instance, in Fig. 16 we show the rain of particles falling off into the formed clumps. It is interesting to note that there is a very marked fall in the angular momentum value only when the particles are really close to the densest clump, as it can be appreciated in Fig.17. It is therefore the particles of the innermost disk which are the most relevant for the momentum interchange.

We clarify that in Fig.17 a dot corresponds to a *SPH* particle of the simulation; thereby, the shaded region in these plots indicates an important accumulation of particles.

3.5. Energy ratios.

As we previously mentioned in Section3.2, our collapse models stop evolving when the first formed matter aggregates reach a peak density around 10^{-11} gr/cm^3 . Those gas aggregates can be identified as protostellar cores, already. Nowadays, it is well established that these protostellar cores physical characteristics are more likely to be inherited by the stars that might result from them if they could collapse further until peak densities around 10^{-1} gr/cm^3 are reached. It is therefore very important to study those protostellar aggregates physical properties, as we do below.

3.5.1. Defining fragments.

We define the center, \vec{x}_{center} , of a matter aggregate as the particle with the highest density in the region where the aggregate is located. We then find all the particles, let us say N_s , which have a density above (or equal to) some minimum density value ρ_{min} and which, at the same time, are located within a given maximum radius r_{max} from the aggregate center. We can define a region of matter with this set of N_s particles from which we can estimate the integral properties, as it will be escribed in Section3.5.2. When the two cutting parameters, ρ_{min} and r_{max} , are taken into account at the same time for selecting particles, then the aggregate of matter will be referred as a *fragment*. We plot the centers of these matter aggregates in Fig. 18, for each simulation.

3.5.2. Calculation procedure.

We now show the way in which we can estimate the energy ratios α and β for a set of N_s particles defining a fragment. The first step is to obtain the density and the gravitational potential for every particle i due to the presence of all others particles $j \neq i$.

We use the smoothing kernel for calculating the particle density i by means of $\rho_i \equiv \rho(\vec{r}_i) = m W_1(\vec{r}_i, h)$, where $W_1(\vec{r}_i, h)$ is the spline kernel given in Eq. A.1 of Springel et al. (2001). We use another kernel for the gravitational potential, such as $\Phi_i \equiv \Phi(\vec{r}_i) = G \frac{m}{h} W_2(\frac{\vec{r}_i}{h})$, where the kernel W_2 is now given in Eq. A.3 of the same reference. The softening length h appearing in these two kernels sets the neighborhood on the point \vec{r} , outside of which no particle can exert influence on \vec{r} ; that is, for $r > h$ both kernels vanish: $W_1 \equiv 0$ and $W_2 \equiv 0$. We use several values for h , looking forward to have a number of neighbor particles for any point (or particle) greater than or equal to 50.

We approximate the thermal energy of the clump by calculating the sum over all the N_s particles, that is

$$E_{therm} = \sum_{i=1}^{N_s} \frac{3}{2} \frac{P_i(\rho) m_i}{\rho_i}, \quad (12)$$

where P_i is the pressure associated with particle i with density ρ_i by means of the equation of state given in Eq. 6. Similarly, the approximate potential energy is

$$E_{pot} = \sum_{i=1}^{N_s} \frac{1}{2} m_i \Phi_i. \quad (13)$$

Although a bit more complicated, the rotational energy of N_s particles can be calculated as follows with respect to the Z -axis of the located clump. Let \vec{x}_i and \vec{v}_i be the position and velocity of particle i in the gadget2 coordinates. Thereby the coordinates of those particles in the clump with respect to the clump center are $\vec{u}_i = \vec{x}_i - \vec{x}_{center}$. The azimuthal angle ϕ_i associated with the particles rotation with respect to the Z -axis can be calculated by taking the ratio of particle coordinates projection with the unitary vectors $\hat{i} = (1, 0, 0)$ and $\hat{j} = (0, 1, 0)$, that is $\phi_i = \arctan(\vec{u}_i \cdot \hat{j} / \vec{u}_i \cdot \hat{i})$. The rotational energy can be thus estimated by taking the projection of the velocity along the unitary azimuthal vector $\hat{e}_{\phi_i} = -\sin(\phi)\hat{i} + \cos(\phi)\hat{j}$, that is

$$E_{rot} = \sum_{i=1}^{N_s} \frac{1}{2} m_i (\vec{v}_i \cdot \hat{e}_{\phi_i})^2. \quad (14)$$

3.5.3. Calculated properties for fragments.

We arbitrarily chose the cutting density $\rho_{min} = 1.40 \times 10^{-17} \text{ gr/cm}^3$ for defining a clump, which corresponds to 100 times the cloud average density

for model *A3*, see Table 1. Any clump with this cutting density will in general include about 1.5% of the total number of particles in the simulation.

We sum to the mass and to the forming clump angular momentum, going forward through as many snapshots as possible in each simulation, the contribution of all those particles having a density higher than ρ_{min} . As a matter of fact, we show in Fig. 19 how the angular momentum and the mass of the clump evolve as more particles enter into the forming clump. We have added a C in these plots to emphasize that we are not only using the second cutting parameter r_{max} . The left panel shows the specific angular momentum, while the right panel shows the *aem* ratio. We see that very few particles in model *A0* reach densities higher than ρ_{min} long before other particles; whereas in model *A3*, the collapse is more uniform, in such manner that many more particles come to be part of the forming clump at the same time.

Another observation from these two panels of Fig. 19 is that as the gas envelope extension increases, the specific angular momentum increases as well, but the *aem* ratio decreases. This is because the first particles joining the forming clump bring more angular momentum than those particles that collapse afterwards, which provide more mass to the clump than angular momentum. As the *aem* ratio is more sensitive to the mass contained in the clump, the *aem* ratio magnitude falls as the new clump is forming.

Moreover, Fig. 19 indicates that in the model *A3* more particles are still located in the envelope, and most of them are still keeping a large angular momentum, as it can be seen in Fig. 14; meanwhile, a higher proportion of particles have already entered the phase of most advanced collapse in the model *A0* and, as a consequence, have already lost most of their angular momentum.

We report the energy ratios calculated by using the two cutting parameters and by the application of the calculation procedure outlined in Section 3.5.1 to the last snapshot obtained for each simulation in Table 3. The entries of Table 3 are as follows. We show the model label for which we are going to account for only the formed central clump in column 1. We indicate the number of particles (N_s) entering into the set of particles used for approximating the energy ratios calculation in column 2. We show in columns 3 and 4 the energy ratios α_f and β_f as previously defined in Section 3.5.2. We emphasize that the minimum density values expressed in terms of the $\log_{10}(\rho_{min}/\rho_0)$ have been taken to be 4.0 for all the models; this is the lowest value that a particle entering in the set can indeed have. Moreover, we indicate the maximum radius expressed in terms of the size of the simulation box, $2R_0$, which was fixed to 0.01 in order to delimitate the clump radial extension.

3.5.4. Global Properties.

As we have already applied the procedure outlined in Section 3.5.2 in previous publications, it is now clear that the numerical results for the energy ratios unfortunately depend on the values chosen for the two cutting parameters, ρ_{min} and r_{max} , as we inevitably commit certain ambiguity in defining the

clump boundaries. Furthermore, with this procedure we obtained information only about the physical state of each clump or fragment, separately.

We calculated the energy ratios in this section using all the particles in each simulation, to avoid cutting ambiguities. We follow again as in the previous Section 3.5.2, but in this case, we have $N_s = N$. We have added the subscript w on the plot, to distinguish those quantities calculated when using all the simulation particles.

It is important to emphasize that there is a clear advantage in taking all the particles for this calculation, as the new clumps formation resulting from the gravitational collapse can be recorded in the behavior of the α and β variables, as we will describe in this Section.

When a clump begins to form, the pressure of their constituent particles increases, and we would expect that the α variable would also show an increase in spite of the fact that the gravitational potential is also growing in magnitude. Since now we do not care where the particles are located in the cloud for the purpose of measuring the α and β values, we can capture the formation of new clumps wherever they start. We therefore have a tool for recording an imprint left by the occurrence of fragmentation in the cloud on these dynamical variables.

Let us take a look at Fig. 20, where the curves behavior α vs β are somewhat different for each simulation, indicating the different outcomes of each cloud model. However, in these panels there are clearly common features in all the curves, establishing a very strong similarity between the pairs of models A0 with A1 and A2 with A3. This association in pairs of models is obviously a consequence of the gas envelope extension on the simulation outcome.

There is a first stage marked by the labels 1 and 2, which points to the fact that the early collapse evolution of all the cloud models proceeds in an identical manner; in this first stage the α is decreasing as a consequence of the systematic increase of the gravitational potential for the cloud central particles. The 1-2 stage takes about a free fall time for each cloud, at a time at which the cloud central part has already lost its initial spherical symmetry, because the densest particles have found a place in a narrow slice of matter (the filament) around the equatorial plane, occupying approximately up to 10 % of the original cloud size. The upper left panel of Fig. 5 corresponds to the end of this first stage 1-2, as it is indicated in the panel labeled with A0 of Fig. 20.

Let us now define with the labels 2-3, a second stage in the α vs β curves evolution, in which there is a pronounced increase of the α values. At this stage, which will also occur on all the models, new clumps are starting to form out. We notice indeed the appearance of two small over-dense clumps in each extreme of the prolate cloud central region, which were planted by means of Eq. 3. Shortly after, we noticed that these small clumps get connected by a very well defined bridge of particles. As an instance, for the first pairs of models A0 and A1, this 2-3 stage has been illustrated with the second and third panels of Fig. 5 and the second panel of Fig. 6, respectively.

Later on, we notice that the formation of large spiral arms surrounding the central clump in models *A0* and *A1*, has the consequence of an increase in the β value, giving place to a third stage in the α vs β curves evolution, labeled as 3-4 in Fig. 20. As the mass of the central clump increases, the centripetal force acting on the gas should also increase for those particles with a small radii, pointing out to a strong increase in the rotational energy.

We observe in Fig. 20 that the 3-4 stage does not occur neither in model *A2* nor in *A3*, despite of the fact that we observe that spiral arms are also formed in these models, although with a much smaller extension that in models *A0* and *A1*.

There is still a 4 stage for the pairs of models *A0* and *A1*, labeled by 4-5, in which both the α and the β values decrease, indicating that the cloud central region is losing both thermal and rotational energy. The main dynamic event occurring at this stage is the merger of the two clumps already formed, as illustrated in the bottom right panel of Fig. 5 for model *A0*, and the bottom left panel of Fig. 6 for model *A1*.

We finish the dynamic description of models *A0* and *A1* by noticing that there is a last stage of the curve after the point 5 label, in which we observed the formation of *exterior* clumps resulting from the spiral arms breakage.

There is also a last stage for models *A2* and *A3* manifested in the rattle behavior of the α vs β curve, just after label 2, where we see the cloud fragmentation by means of tiny clumps being formed around the central original clump. For instance, in model *A2*, a gas ring surrounding a central clump formed at the end of the first stage (see the fourth panel of Fig. 7) now begins to fragment, as it can be better appreciated in Fig.9 of Arreaga et al. (2010). We also recognize the cloud central region fragmentation occurrence for model *A3*, as it can be seen in the last panel of Fig. 8.

4. DISCUSSION

We have tried in the Paper hereby to make a link between a simulation and the behavior of its associated dynamic variables; particularly, with the angular momentum, the *aem* ratio and with the α and β parameters. Mainly in Section 3.5.4 we have shown the way in which the most important dynamic events of each simulation considered here are manifested and recorded in the α and β curves displayed in Fig. 20.

We have established pairs of simulations due to the similarities recognized in their α vs β curves, pointing out strong dynamical similarities between the models *A0* with *A1* and between the models *A2* with *A3*. However, there are significant dynamical differences even among a single pair, which are noteworthy.

We consider now in this Section some characteristic events of each simulation, and show how these events can be a consequence of either the gas envelope extension or the simulation initial conditions. We would like to emphasize here how these events are caused by (or manifested on) the dynamical variables describing the cloud evolution.

4.1. *The merging issue of the early densest clumps*

The merging process described in Section 3.5.4 is a very important dynamical characteristic observed for the pair of models *A0* and *A1*, where two clumps, each formed near the filament end, merge into one single central matter clump.

As we have implemented a symmetric mass perturbation with respect to the origin of coordinates of the cloud equatorial plane, the seed clumps that will form will be antipodes of each other, in such a manner that an imaginary line joining them will pass through the coordinates origin, too. Thus, every clump exerts a gravitational torque on the other clump. The particles velocity in either clump begins to align with the imaginary symmetry axis joining the clumps, that is, $\vec{v} \approx \vec{r}$, with the net effect that these particles lose angular momentum. Next, the particles which are accreted into the clumps are the the ones with lower angular momentum, whereas those accreted into the surrounding spiral arms are those with higher angular momentum. As the clumps lose their total angular momentum, the gravity force that every clump exerts on the others brings them closer until they finally merge.

The benchmark of uniform density cloud collapse is the development of a gas filament with a small gas clump located at each filament end. Indeed, Arreaga et al. (2008) have considered a model (labeled as UA), which is very similar to the present model A0. It is observed in these models that the filament becomes shorter in time due to the gravitational attraction between the small gas clumps at its ending points. The models outcome are different at the final evolution stage, for we observed the formation of a binary system in model UA and only one central clump in model A0. We may also mention another simulation reported by Bate *et al.* (1995), in which the closeness among the clumps was observed, but not the final merging. In those works, the clumps pass by each other without merging, settling into an orbit around each other.

The reason behind the different behavior, which may decide whether merging occurs or not, is perhaps due to the existence of small variations in the particles positions and velocities, coming from the randomness of the initial particle distribution, whose origin is the density perturbation in Eq. 3, which turns out to play a very important role in this merging issue. Indeed, the mass perturbation is the cause for the two small regions development.

Once the cloud has acquired a flattened configuration, the higher density gas will form an elliptical structure with these small accretion regions, at the focal points. As demonstrated by Burkert & Hartmann (2004), the fate of this elliptical structure is always to collapse into a filament with a strong mass accumulation at each ending point.

4.2. *The development of spiral arms*

The differences in the spiral arms development are in the extension and in the spiral arms breakage level, as it can be appreciated by looking at Fig. 15.

We have observed the formation of very large and massive spiral arms for model *A0*. We still see the formation of well defined spiral arms for model *A1*, but now the particles circular motion is somewhat distorted at the spiral end regions, which may be a warning sign of the forthcoming breakage. The spiral arms for models *A2* and *A3* are thin and short, but still well defined.

Curiously, the spiral arms are able to fulfill a complete turn around the central clump, in models *A2* and *A3*, indicating that there are more particles being accreted as well onto the gas ring formed from the spiral arms rather than directly onto the central clump. We then find that the gas ring has a very short life term in the case of model *A3*, while the lifetime is longer for model *A2*.

The key for understanding such different behavior in our simulations, comes from Section 2.3. It was shown there that the total rotational energy of the assembled cloud must be shared between the core and the envelope. We reported in Table 2 that the rotational energy remaining in the core was decreasing as the gas envelope mass was growing. We claim that this core rotational energy is responsible for the cloud spiral arms growth; consequently, that it was ultimately the reason behind the different outcomes in the simulations, whereas for the pairs of models *A0* and *A1*, the rotational energy left in the core is enough for the spiral arms formation, while for the pair of models *A2* and *A3*, it is not.

4.3. *The fragments virialization issue*

We showed in Section 3.5.4 that when we include all the simulation particles in the calculation of the energy ratios α and β , the curves do not show any trend to approach the virial line. We would conclude in this case that neither the resulting fragments nor the cloud itself virialize, and that the cloud collapse is still in progress. We emphasize that we have not followed the subsequent simulation time evolution because the time-step of the run becomes extremely small, to the point of being almost incapable of advancing the simulation particles forward in time.

However, when we calculated the α and β values taking into account only those particles satisfying the cutting parameters, as defined in Section 3.5.3, we observe that the clumps do show a clear tendency to virialize, as it can be appreciated in Table 3. We emphasize that a similar conclusion can be drawn from the calculation of Arreaga et al. (2008), where plots of the α and β time evolution were presented.

5. CONCLUSIONS.

We carried out in this paper a full set of three dimensional numerical hydrodynamical simulations, in order to theoretically study the sensitivity of the gas core gravitational collapse on the extension of a gas envelope surrounding the core at a high spatial resolution, with a barotropic equation of state and within the framework of the *SPH* technique. We have also used

several dynamical variables aiming to characterize the simulation results and the collapsing process itself. What we have observed in this paper can be summarized as follows:

- A bigger gas envelope delays much longer the collapse; however, the collapse is more homogeneous as many particles reach higher densities at the same time, see Fig. 9.
- The larger the gas envelope extension, the larger the radius of the gas ring surrounding the central densest clump; a region which shows resistance to the collapse, due to the combination of both thermal and centrifugal effects; see Fig. 10.
- The gas envelope radial extension does not affect the radial profile behavior of the specific angular momentum and aem ratio as we only observed changes in the magnitude, but the same trend for all the models; see Fig. 12 and 13.
- For the models with higher gas envelope extension, the particles falling into the central densest clump are losing angular momentum as well as aem ratio even though those particles have not reached densities as high as those in the models with less gas envelope extension; see Fig.14.
- The smaller the gas envelope extension, the larger the spiral arms extension; Fig.15.
- The larger the gas envelope extension, the smaller the central densest clump spatial extension and, consequently, the longer the paths followed by the accreting particles; see Fig.16.
- The larger the gas envelope extension, the smaller the spatial extension of the central cloud region around the forming densest clump, where a strong influence on the loss of angular momentum and aem ratio of the accreting particles, is observed; see Fig.17.
- The gas envelope extension length can drastically change the simulation final outcome; see Fig. 18.
- As the gas envelope extension increases for the forming clump, the specific angular momentum also increases, but the aem ratio decreases; see Fig. 19.
- The β ratio maximum values, as well as the α ratio minimum values, reached during cloud contraction, are both somehow regulated by the gas envelope extension; see Fig. 20.

Acknowledgments

GA. would like to thank ACARUS-UNISON for the use of their computing facilities in the making of this paper.

REFERENCES

- G. Arreaga, J. Klapp, L. Sigalotti and R. Gabbasov, 2007, *ApJ*, **666**, 290-308.
- G. Arreaga, J. Saucedo, R. Duarte and J. Carmona, 2008, *RMAA*, **44**, Num. 2, 259-284.
- G. Arreaga, J. Klapp, and F. Gomez, 2009, *A&A*, **509**, pp. A96.
- Bate, M.R., Bonnell, I.A., Price, N.M., 1995, *MNRAS*, **277**, 362.
- Boss, A.P. and Bodenheimer, P., 1979, *ApJ*, **234**, 289.
- Boss, A.P., 1987, *ApJ*, **319**, 149.
- Boss, A.P., 1991, *Nature*, **351**, 298.
- Boss, A.P., Fisher, R.T., Klein, R., McKee, C.F., 2000, *ApJ*, **528**, 325.
- Bodenheimer, P., 1995, *ARA&A*, **33**, 199
- Bodenheimer, P., Burkert, A., Klein, R. I. & Boss, A. P. 2000 in *Protostars and Planets IV*, ed. V. G. Mannings, A. P. Boss, & S. S. Russell (Tucson: University of Arizona Press), 675
- Bouwman, A.P., 2004, *Astrophysics and Space Science*, **292**, 325.
- Burkert, A., Bodenheimer, P., 1993, *MNRAS*, **264**, 798
- Burkert, A., Bodenheimer, P., 1996, *MNRAS*, **280**, 1190
- Burkert, A., Hartmann, L., 2004, *ApJ*, **616**, 288.
- Felice, F. and Sigalotti, L.D., 1992, *ApJ*, **389**, 386-391.
- Goodman, A.A., Benson, P.J., Fuller, G.A., Myers, P.C., 1993, *ApJ*, **406**, pp.528-547.
- Lin, M.K., Krumholz, M. and Kratter, K.M., 2011, submitted to *MNRAS*, arXiv:1105.3205.
- Myers, P.C., 2005, *ApJ*, **623**, 280.
- Natarayan, P. and Lyndell-Bell, D., *MNRAS*, **286**, 268.
- Plummer, H.C., 1911, *MNRAS*, **71**, 460.
- Sigalotti, L.D. and Klapp, J., 1994, *MNRAS*, **268**, 625-640.
- Sigalotti, L.D. and Klapp, J., 1996, *MNRAS*, **281**, 449-462.
- Sigalotti, L.D. and Klapp, J., 1997, *A&A*, **319**, 547-560.
- Sigalotti, L.D., Klapp, J., 2001, *International Journal of Modern Physics D*, **10**, 115.
- Springel, V., Yoshida, N. and White, D.M., 2001, *New Astronomy*, **6**, 79-117.
- Springel, V., 2005, *MNRAS*, **364**, 1105
- Tafalla, M., Mardones, D., Myers, P.C., Caselli, P., Bachiller, R., Benson, P.J., 1998, *ApJ*, **504**, 900.
- Tsuribe, T., 2002, *Progress of Theoretical Physics Suppl.*, **147**, 155-179.
- Tsuribe, T. and Inutsuka, S., 1999, *ApJ*, **523**, L155.
- Tsukamoto, Y. and Machida, M.N., 2011, submitted to *MNRAS*, arXiv:1105.3314.
- Whitehouse, S.C., Bate, M.R., 2006, *MNRAS*, **367**, 32.
- Whithworth, A.P. and Ward-Thompson, D., 2001, *ApJ*, **54**, 317.
- Zinnecker, H., 2004, *Rev.Mex.Astron.Astroph.*, **22**, 77-80.

Centro de Investigación en Física de la Universidad de Sonora, México,
 Apdo. Postal 14740, C.P. 83000, Hermosillo, Sonora, Mexico. (garreaga@cajeme.cifus.uson.mx)

TABLE 3
ENERGY RATIOS FOR THE CENTRAL FRAGMENT.

Model	N_p	$ \alpha_f $	$ \beta_f $	$ \alpha_f + \beta_f $
A0	689951	0.22	0.18	0.4
A1	248831	0.25	0.20	0.45
A2	109924	0.27	0.13	0.4
A3	119326	0.25	0.24	0.49

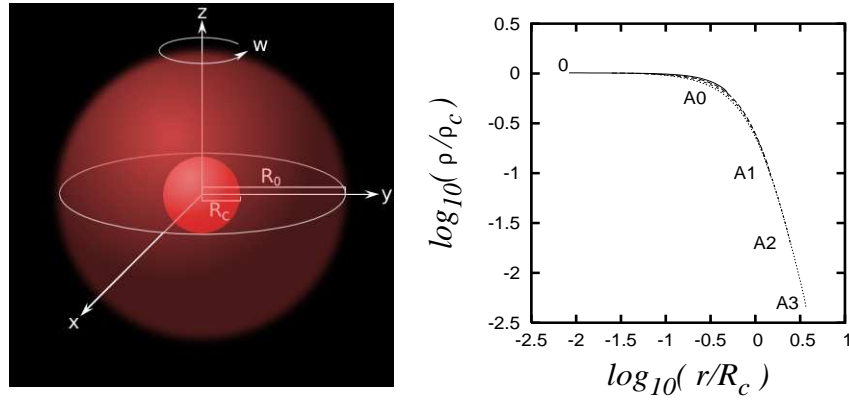


Fig. 1. The model of a cloud composed by a dense core surrounded by an envelope (left) and the radial density profile measured for the initial configuration of particles (right). The radial extension marked in each curve is different according to the model.

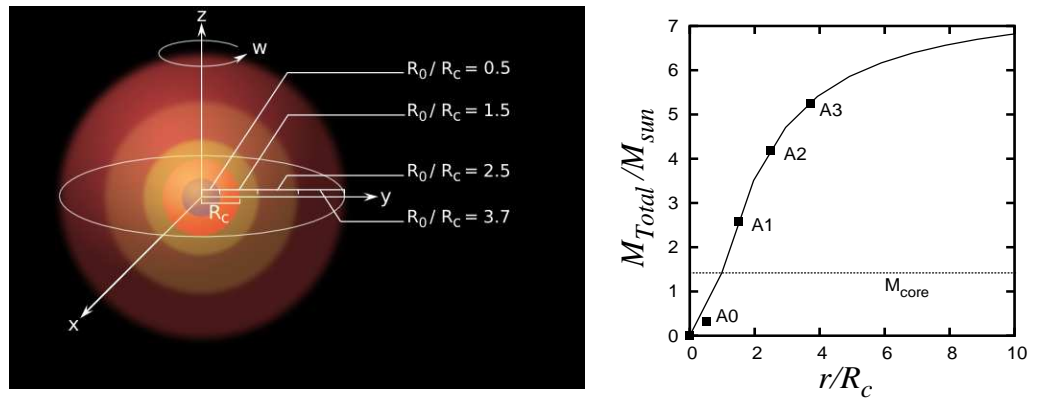


Fig. 2. Schematic representation of the cloud models indicating the extension of the gas envelopes (left) and the mass contained in the cloud (from integration of the Plummer function [solid line] and from the initial configuration of *SPH* particles [black squares]) as a function of radius (right).

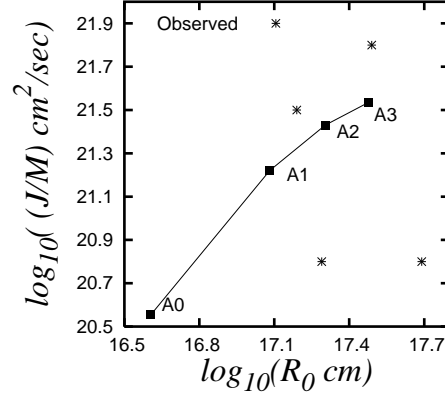


Fig. 3. The initial specific angular momentum J/M against the cloud radius R_0 for all collapse models. The asterisks mark the values of J/M observed for real clouds, see Goodman et al. (1993); Bodenheimer (1995).

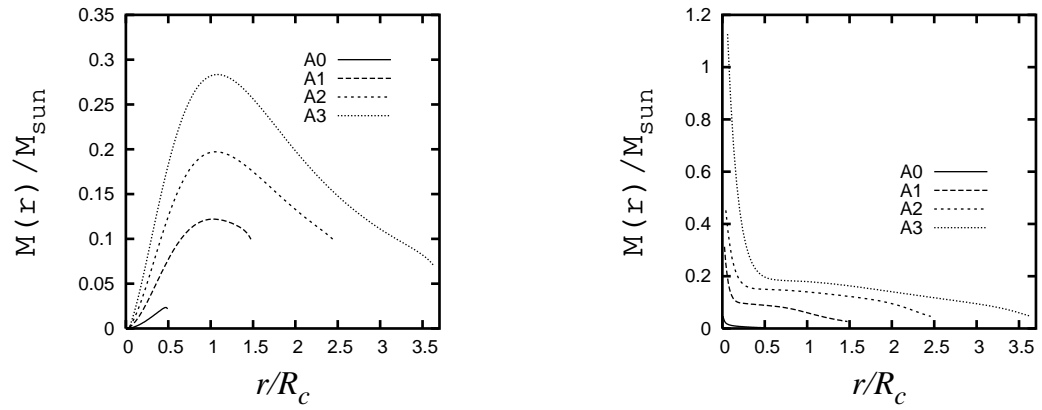
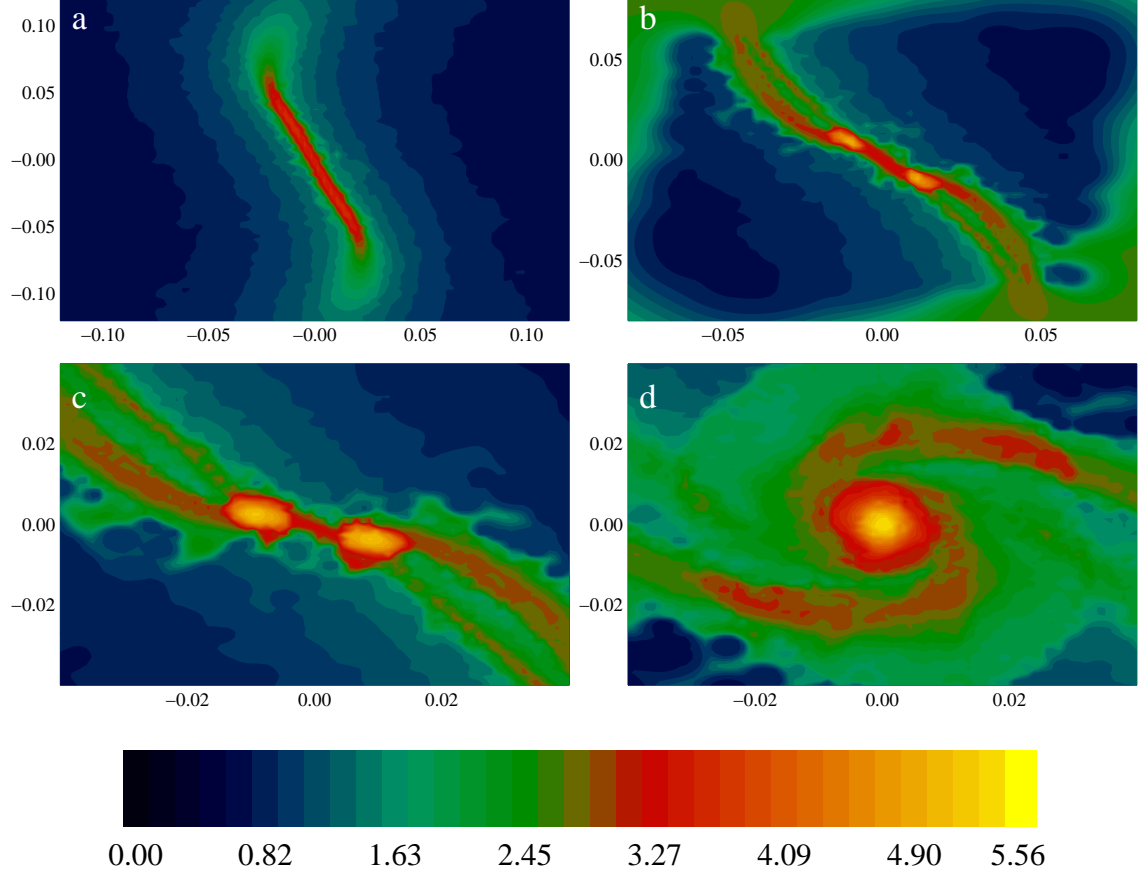


Fig. 4. The radial profile of the mass as a function of the cloud's radius for all models for the initial snapshot (left) and for the last snapshot available (right).



$\text{Log } \rho/\rho_0$

Fig. 5. Isodensity curves of the cloud's mid-plane for model A0 when the distribution of particles reaches a peak density of (a) $\rho_{max} = 3.3 \times 10^{-13} \text{ gr/cm}^3$ at time $t = 1.64 \times 10^{12} \text{ sec}$ (b) $\rho_{max} = 5.8 \times 10^{-12} \text{ gr/cm}^3$ at time $t = 1.66 \times 10^{12} \text{ sec}$ (c) $\rho_{max} = 1.3 \times 10^{-11} \text{ gr/cm}^3$ at time $t = 1.68 \times 10^{12} \text{ sec}$ (d) $\rho_{max} = 2.2 \times 10^{-11} \text{ gr/cm}^3$ at time $t = 1.71 \times 10^{12} \text{ sec}$.

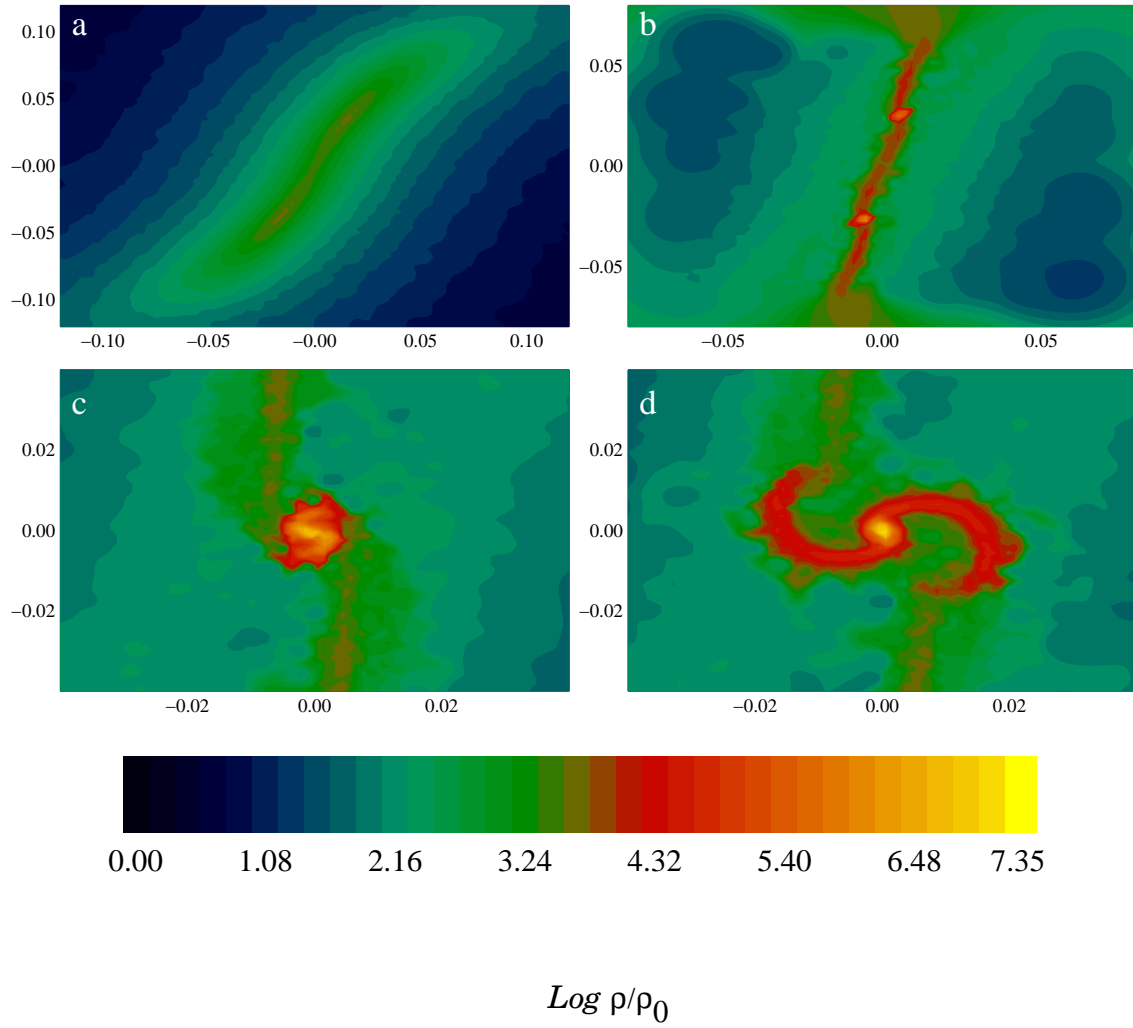


Fig. 6. The same as Fig. 5 but for A1 when (a) $\rho_{max} = 1.15 \times 10^{-14} \text{ gr/cm}^3$ at time $t = 1.78 \times 10^{12} \text{ sec}$ (b) $\rho_{max} = 1.29 \times 10^{-11} \text{ gr/cm}^3$ at time $t = 1.88 \times 10^{12} \text{ sec}$ (c) $\rho_{max} = 3.15 \times 10^{-11} \text{ gr/cm}^3$ at time $t = 1.95 \times 10^{12} \text{ sec}$ (d) $\rho_{max} = 5.29 \times 10^{-11} \text{ gr/cm}^3$ at time $t = 1.96 \times 10^{12} \text{ sec}$.

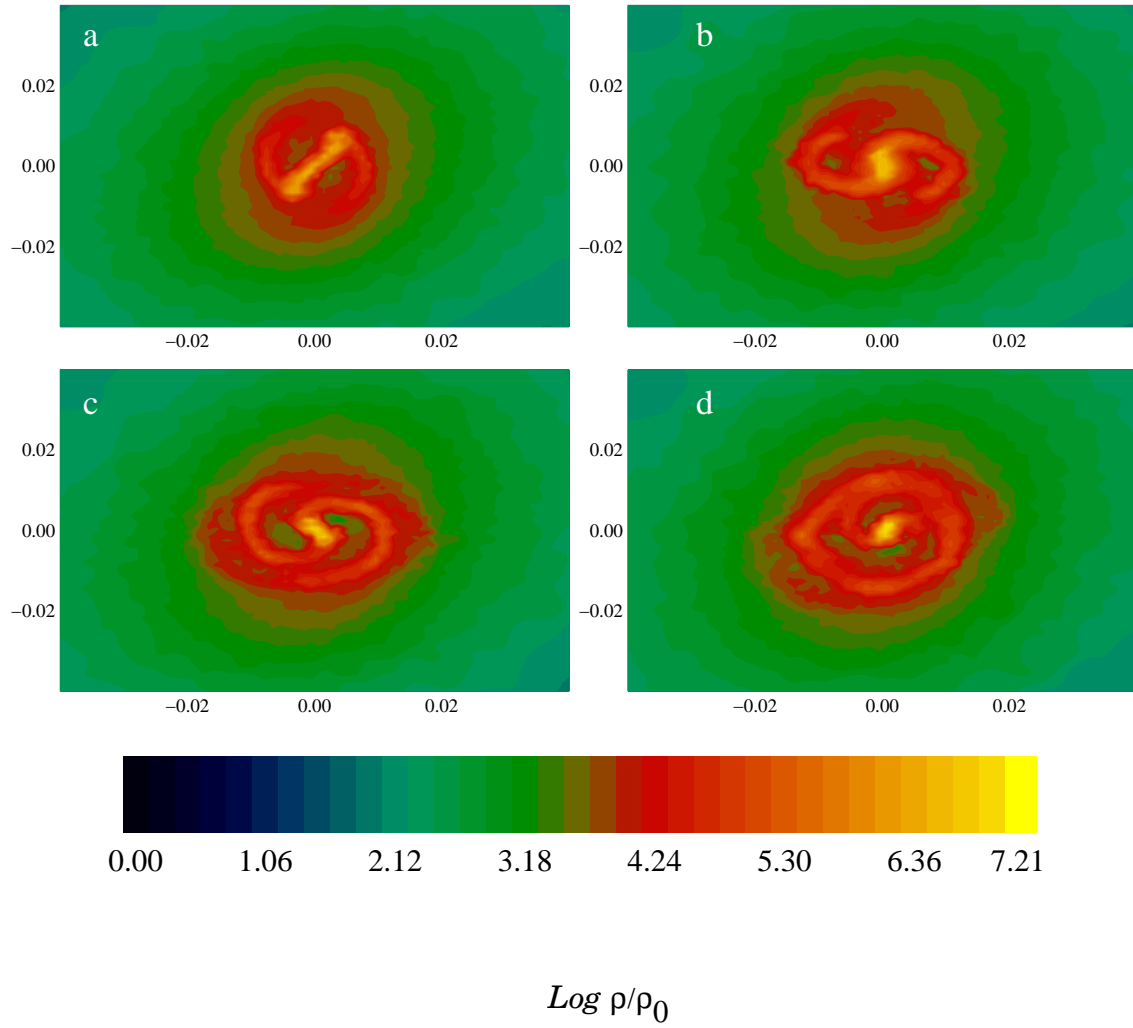


Fig. 7. The same as Fig. 5 but for A_2 when (a) $\rho_{max} = 1.8 \times 10^{-12} \text{ gr/cm}^3$ at time $t = 1.82 \times 10^{12} \text{ sec}$ (b) $\rho_{max} = 4.4 \times 10^{-12} \text{ gr/cm}^3$ at time $t = 1.85 \times 10^{12} \text{ sec}$ (c) $\rho_{max} = 7.1 \times 10^{-12} \text{ gr/cm}^3$ at time $t = 1.87 \times 10^{12} \text{ sec}$ (d) $\rho_{max} = 8.6 \times 10^{-12} \text{ gr/cm}^3$ at time $t = 1.89 \times 10^{12} \text{ sec}$.

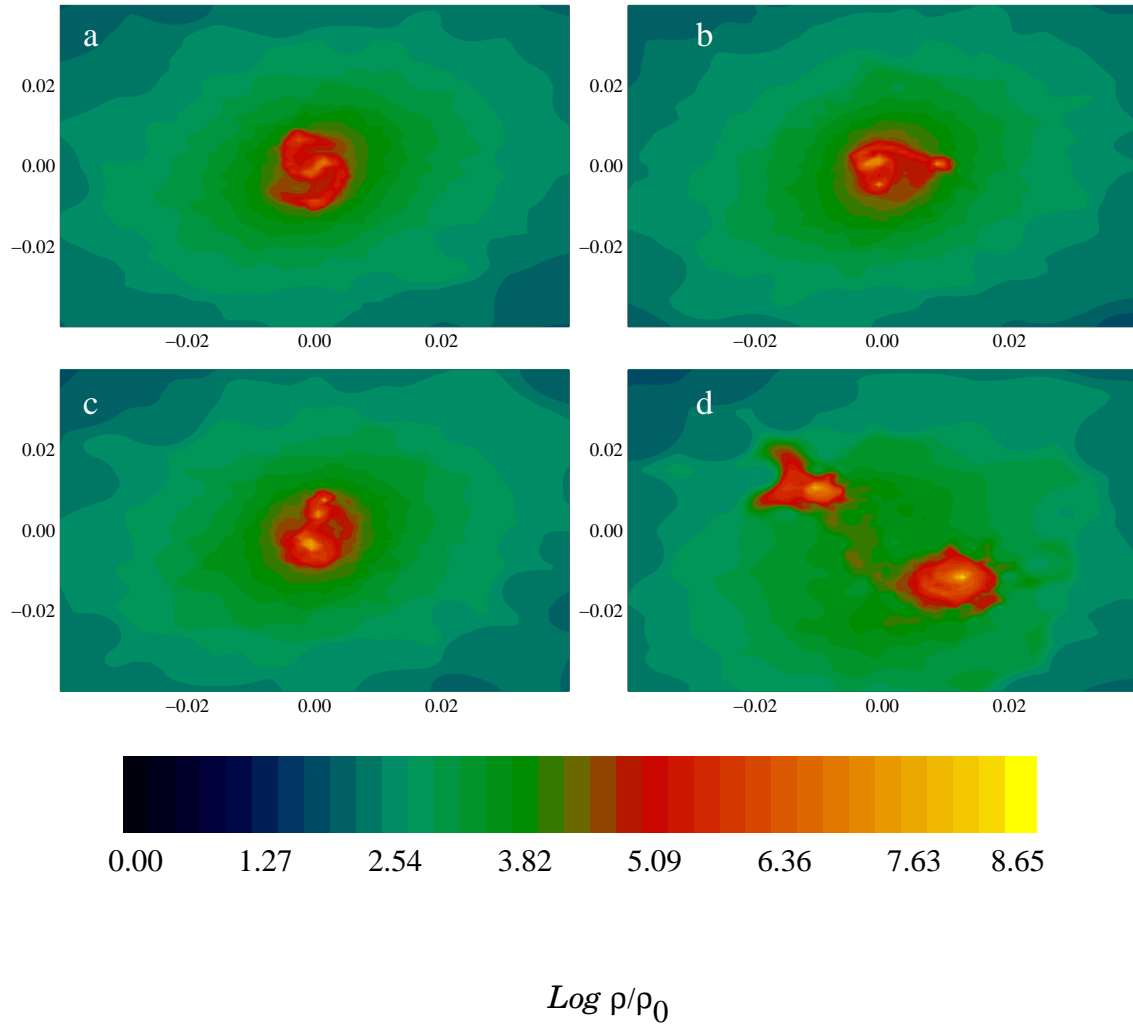


Fig. 8. The same as Fig. 5 but for A3 when (a) $\rho_{max} = 7.74 \times 10^{-12} \text{ gr/cm}^3$ at time $t = 1.82 \times 10^{12} \text{ sec}$ (b) $\rho_{max} = 1.22 \times 10^{-11} \text{ gr/cm}^3$ at time $t = 1.86 \times 10^{12} \text{ sec}$ (c) $\rho_{max} = 1.94 \times 10^{-11} \text{ gr/cm}^3$ at time $t = 1.88 \times 10^{12} \text{ sec}$ (d) $\rho_{max} = 1.67 \times 10^{-10} \text{ gr/cm}^3$ at time $t = 2.19 \times 10^{12} \text{ sec}$.

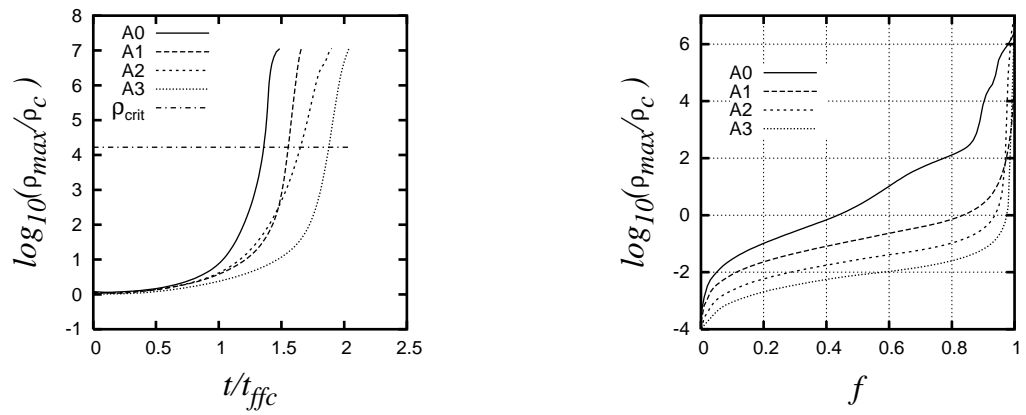


Fig. 9. Time evolution of the peak density of the cloud for all models (left). For the last snapshot available in each simulation, we show the fraction f of SPH particles with a peak density higher than a given peak density as shown in the vertical axis (right).

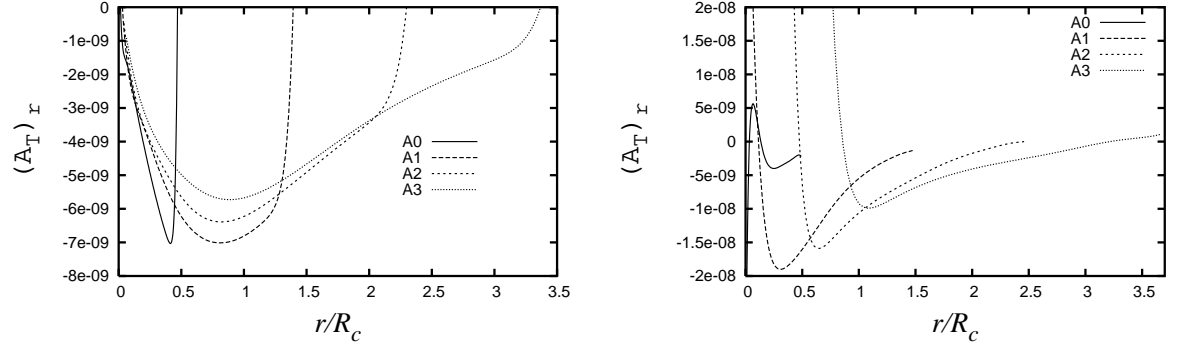


Fig. 10. The radial projection of the total acceleration as a function of the cloud's radius for all models for the initial snapshot (left) and for the last snapshot available (right).

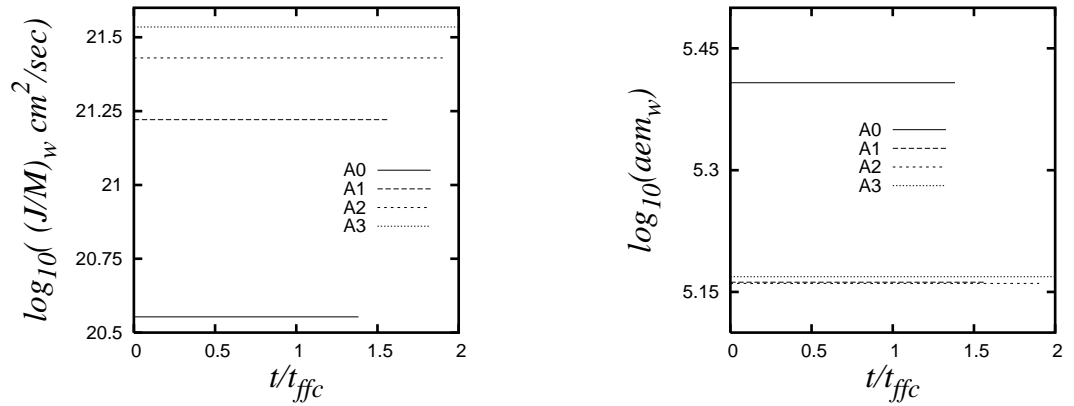


Fig. 11. The time evolution of the specific angular momentum J/M (left) and of the aem ratio (right). Note the good level of conservation of both of these quantities for all the collapse models.

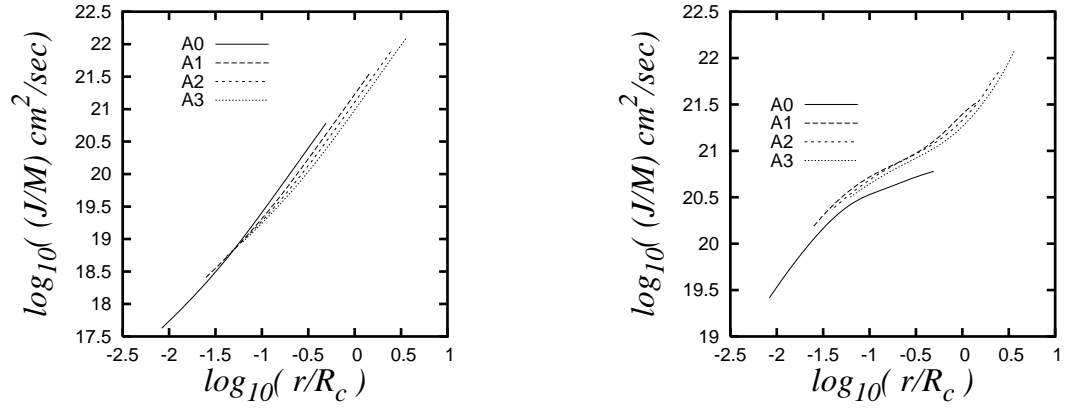


Fig. 12. Radial profile distribution of the specific angular momentum for all collapse models, for the first snapshot (left) and for the last snapshot available (right).

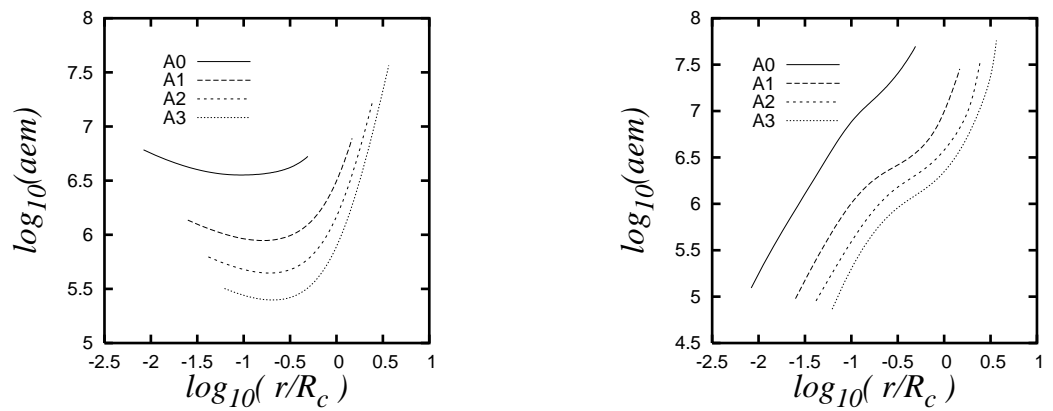


Fig. 13. Radial profile distribution of the *aem* ratio for the initial snapshot (left) and for the last snapshot available (right).

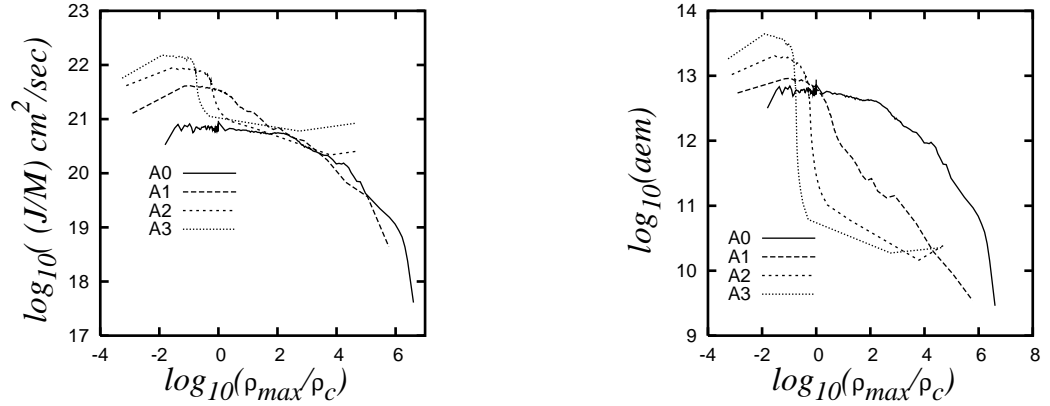


Fig. 14. Distribution of specific angular momentum (left) and *aem* ratio (right) against the density for every particle in the last snapshot available in each simulation.

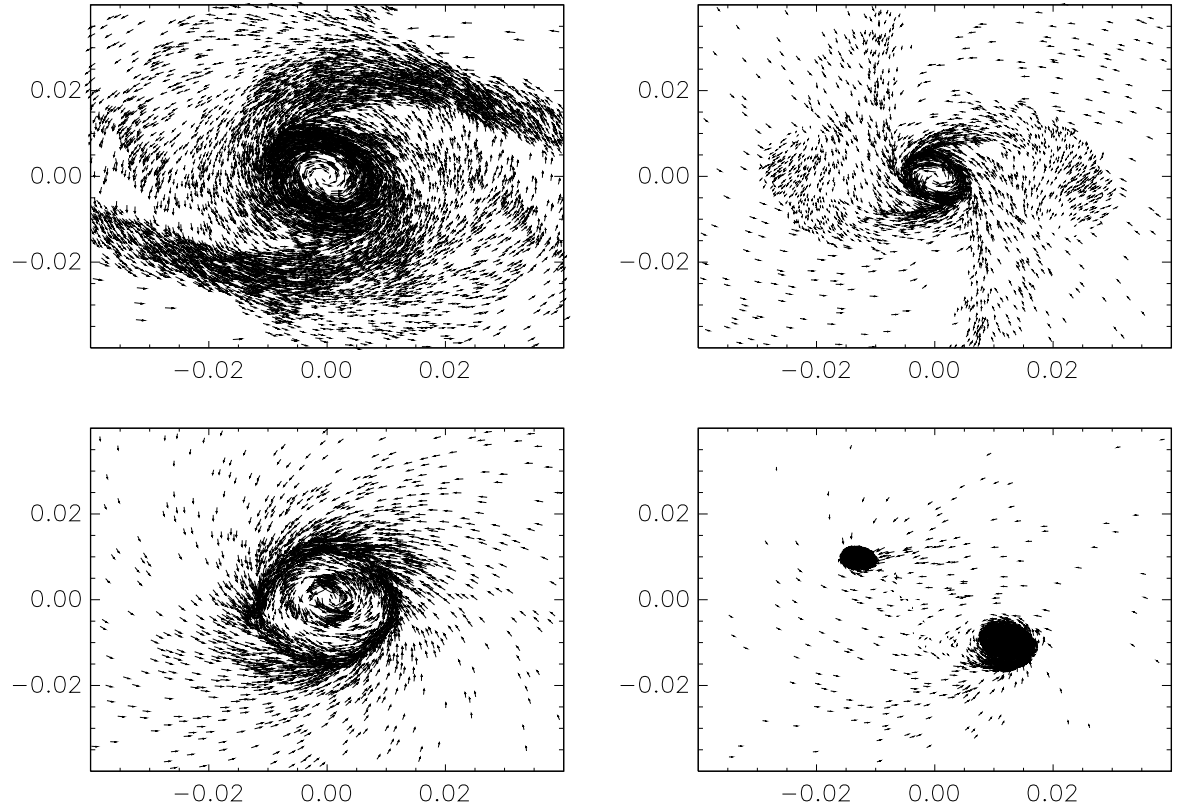


Fig. 15. A 2D plot with the velocity distribution for the final snapshot obtained for each simulation, for model A0 (upper left); for model A1 (upper right); for model A2 (lower left) and for model A3 (lower right). The axes in all of these panels are x/R_c and y/R_c , as is the case in Fig. 16.

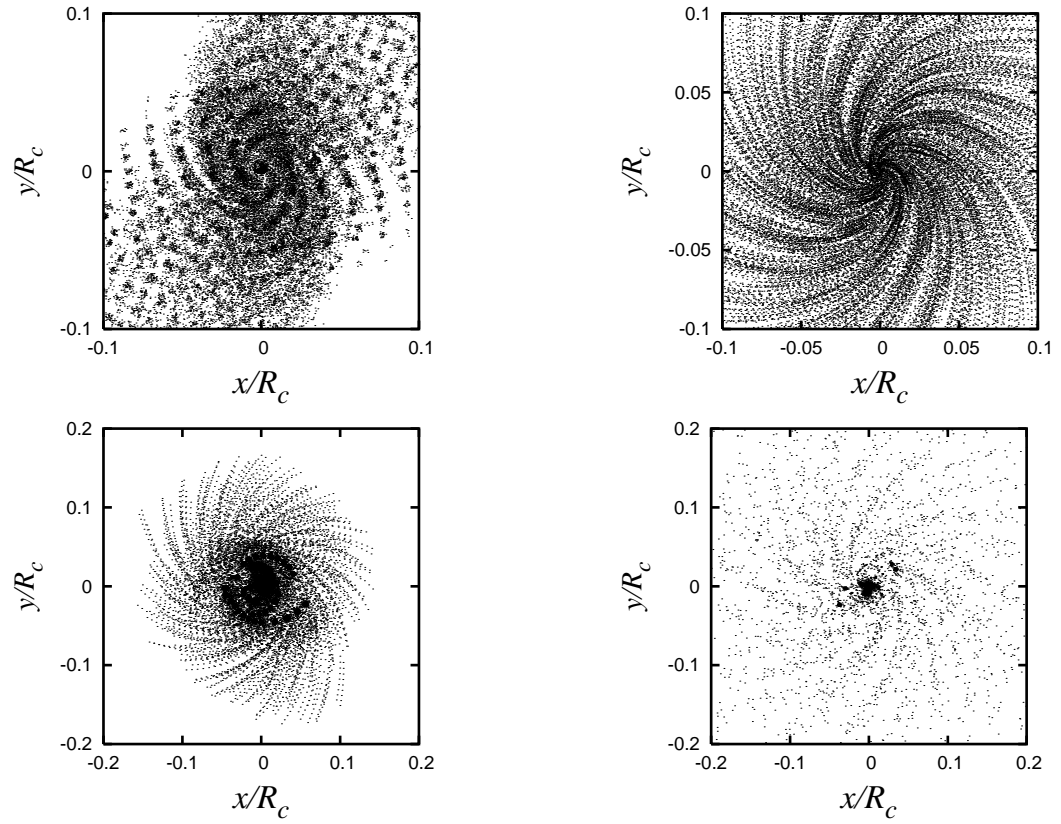


Fig. 16. A 2D view of the path followed by a given set of particles being accreted by the central cloud region, where the densest clumps are forming. Each dot in these plots represents a *SPH* particle of the simulation. The panels here are displayed in the same order that in Fig. 15.

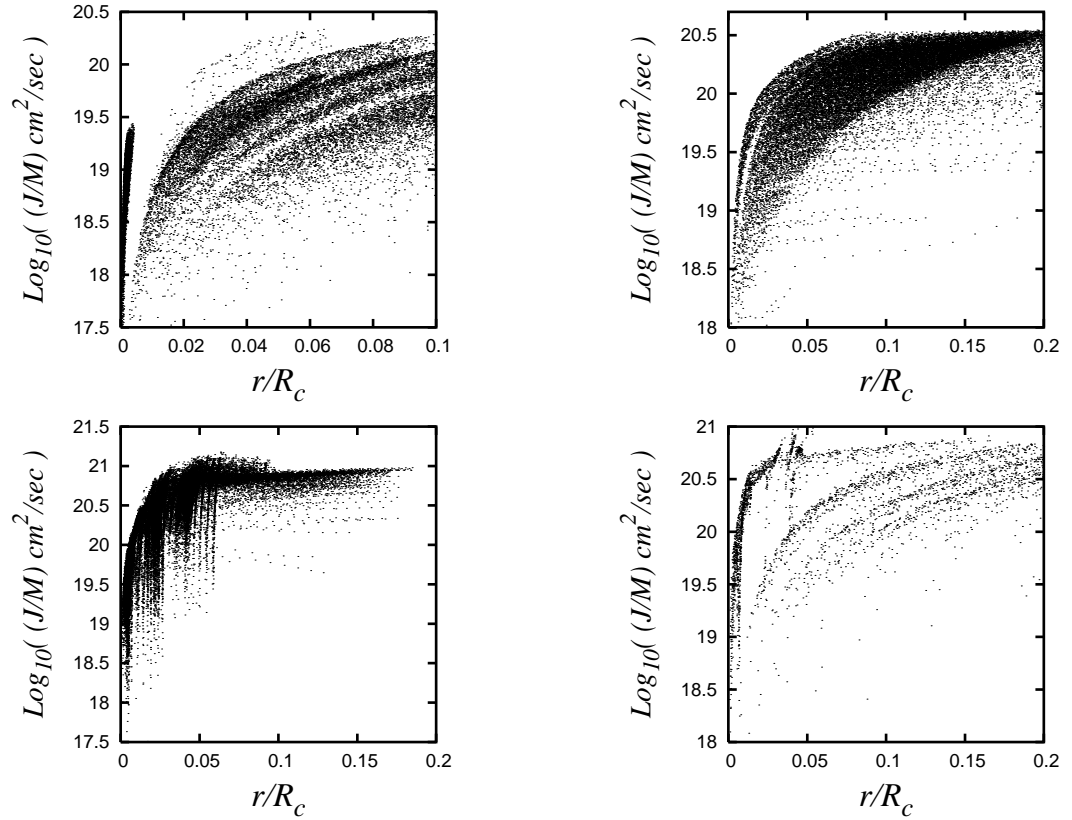


Fig. 17. The specific angular momentum against the radial location for all the particles of the set already shown in Fig. 16. The panels here are displayed in the same order that in Fig. 15.

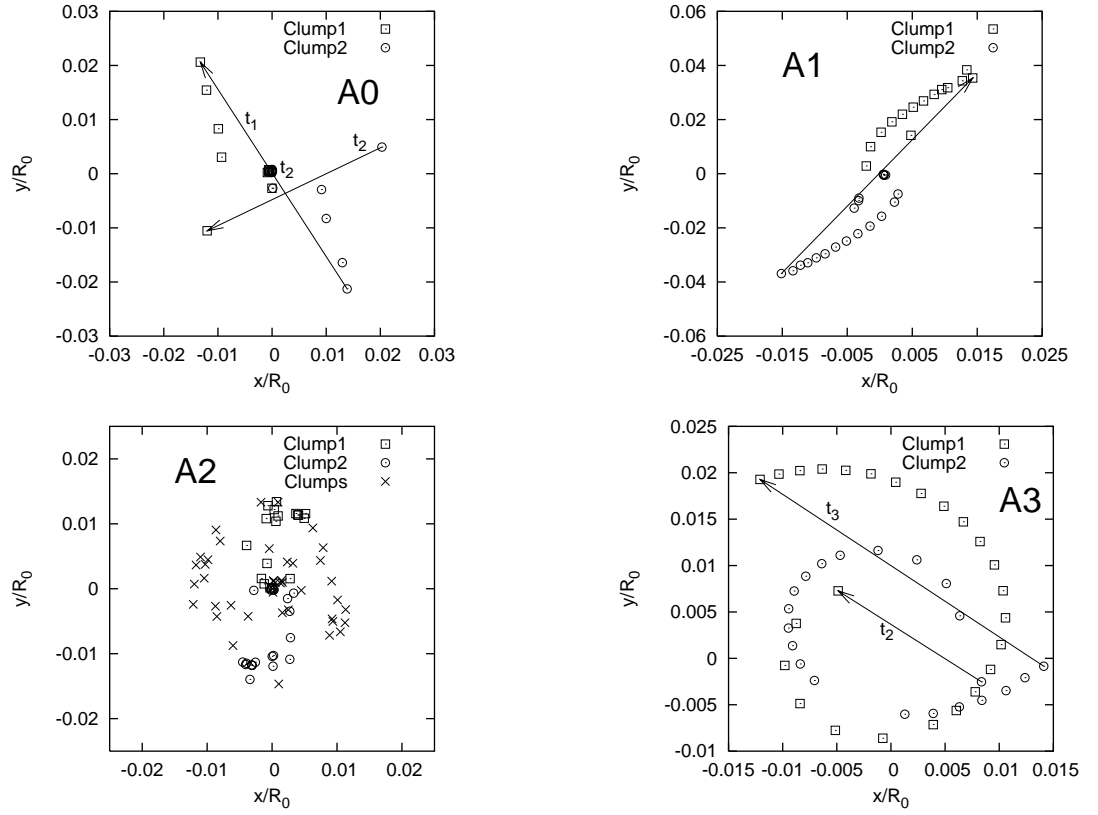


Fig. 18. The path of the centers of clumps already identified for the cloud models. The lines and the time labels attached to them, indicate pairs of fragments observed at the same time. For a given simulation, we always have $t_1 < t_2 < t_3$.

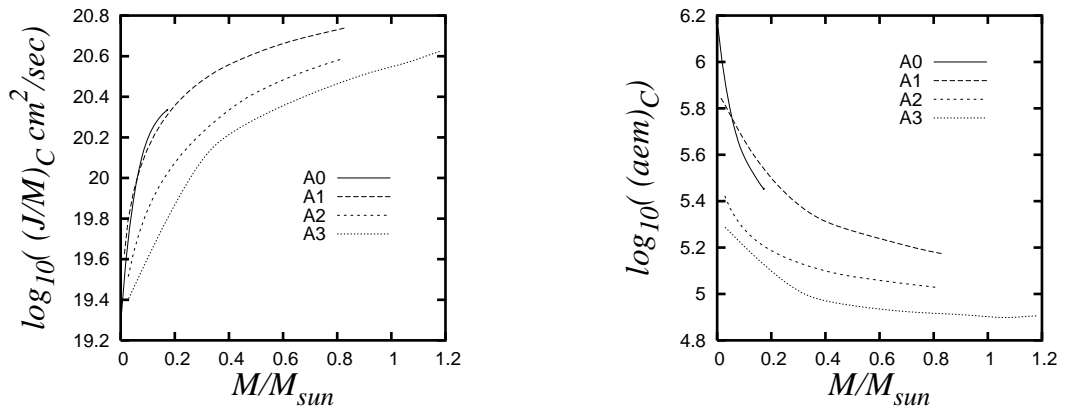


Fig. 19. The angular momentum of the identified clump against the mass of the same clump, including all those particles with a density higher than $\rho_{min} = 1.4 \times 10^{-17} \text{ gr/cm}^3$ for all models.

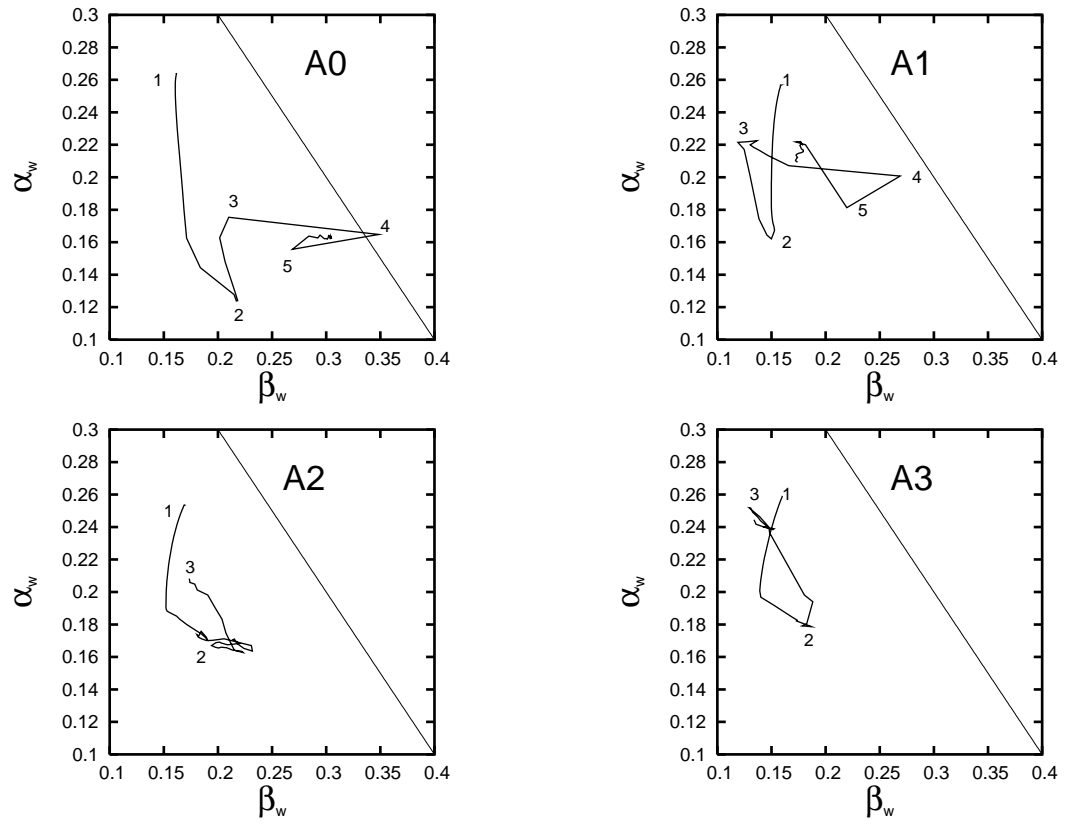


Fig. 20. Energy ratios calculated including all the particles in each simulation. The virial line is shown as a diagonal and continuous line. See Eq. 5.